

PAPER

[View Article Online](#)
[View Journal](#) | [View Issue](#)

Characterization of the geometry of negative dielectrophoresis traps for particle immobilization in digital microfluidic platformst

Cite this: *Lab Chip*, 2013, 13, 1823

H. Rezaei Nejad, Ovee Z. Chowdhury, Matthew D. Buat and Mina Hoorfar*

This paper studies the effect of dielectrophoresis on particle manipulation and immobilization in digital microfluidic (DMF) devices. The dimensions of negative dielectrophoresis (nDEP) traps in the form of circular and square shapes are characterized using numerical and experimental approaches. These efforts will result in defining lifting and trapping zones, the ratio of which is shown to remain constant for trap sizes larger than 40 μm . As a result, a limiting constant K based on the ratio of the particle diameter to the trap size is introduced to identify the status of particle trapping prior to running numerical models or experiments. The results show that K must be less than 0.63 for trapping the particles on the nDEP traps. This study will also result in optimizing the trap size for single particle immobilization which is important for cell printing and growth applications.

Received 22nd November 2012,
Accepted 28th February 2013

DOI: 10.1039/c3lc41292j

www.rsc.org/loc

Introduction

Manipulation, concentration and immobilization of the synthetic (*e.g.*, magnetic beads for immunoaffinity-based isolation)¹ or biological particles (*e.g.*, HeLa cells)² are of interest in many areas of research such as microbiology, environment and biotechnology.^{3–5} Traditional techniques used for concentration and immobilization of particles are time-consuming and often fail to provide reliable results.⁶ Recent efforts have focused on replacing the conventional macro-systems with lab-on-chip (LOC) systems to enhance transport, reaction and manipulation of different species. Over the past decades, LOC systems have contributed to different applications ranging from rapid disease diagnosis,⁷ to cell/DNA separation and manipulation,^{8,9} to environmental monitoring for microbial detection¹⁰ to fabrication of nanowires for micro-circuits.¹¹ The first generations of LOC systems include the etched microchannels for fluid transport. These systems, referred to as continuous microfluidics, require peripheral devices such as micro-pumps or micro-valves to facilitate transport.¹² Another type of LOC systems, emerged in more recent years, is called digital microfluidics (DMF) capable of manipulating the sample in the form of micro-droplets without the need for peripheral devices. Typically, the micro-droplet is confined between two plates, where the top plate is grounded and the bottom plate has an array of

electrodes covered by a layer of dielectric material (such as PDMS or Parylene C).⁹ To increase the hydrophobicity of the bottom layer (facilitating the motion of the droplet) a hydrophobic layer (such as Teflon) is deposited on the dielectric layer. In such devices, various droplet actuation mechanisms such as thermocapillary,¹³ surface acoustic wave (SAW),¹⁴ electrowetting on dielectric (EWOD),¹⁵ dielectrophoresis (DEP),¹⁶ and magnetic force¹⁷ have been introduced. Among different actuation mechanisms, EWOD is the most common method.¹⁸ Regardless of the actuation mechanism, the versatility and reconfigurability of DMF systems make them ideal for integration into a number of applications involving handling and control of bio-particles.

Several methods have been explored for manipulation of target particles flowing with the fluid in continuous microfluidic or within the droplet in digital microfluidic devices. These approaches include optics,^{19,20} acoustics,²¹ electrothermal,²² magnetic,^{23–27} hydrodynamics,²⁸ mechanical filtration,^{29,30} electrophoresis,³¹ and dielectrophoresis (DEP).³² DEP, which strongly depends on the difference between polarizability of the particle and surrounding medium in a non-uniform electric field,³³ has shown high efficiency in particle manipulation without requiring additional elements (such as a magnet or light source). DEP can be observed as positive (pDEP) and negative (nDEP), moving particles toward the high and low intensity electric fields, respectively, depending on the particle and medium dielectric properties as well as the frequency and the degree of non-uniformity of the applied electric field. Although trapping the particles using pDEP traps is easier, for most biological applications requiring a high conductivity buffer medium nDEP traps must be used

University of British Columbia, School of Engineering, EME4281, 3333 University Way, Kelowna, BC, V1V1V7, Canada. E-mail: mina.hoorfar@ubc.ca; Fax: (250) 807-9850; Tel: (250) 807-8804

† Electronic supplementary information (ESI) available. See DOI: 10.1039/c3lc41292j

to preserve the physiological characteristics of the particle by minimizing the stress on the particles and preventing high *trans*-membrane potentials.³⁴ A prodigious number of studies reported different types of nDEP traps mostly in continuous microfluidics including nDEP cages,³⁵ nDEP octopole³⁶ and more recently nDEP planar electrodes which is shown to be effective for single particle patterning in continuous flow microfluidics.³⁷ One of the important factors affecting particle manipulation/trapping using nDEP is the trap geometry. Although there has been a prodigious amount of studies conducted in manipulation of particles using DEP,^{38–40} less studied is the effect of the trap geometry on the efficiency of DEP for particle trapping especially in DMF devices.

In this paper, different nDEP trap geometries will be thoroughly investigated using numerical simulations and experimental studies. A comparison between the high intensity zone (referred to as the lifting zone) and the low intensity zone (referred to as the trapping zone) for different geometries and dimensions will be conducted. The results will show that the geometry design significantly dominates the DEP force as well as the trapping zone created for capturing the particles. As a result, a limiting constant K based on the ratio of the particle diameter to the trap size is introduced to identify the status of particle trapping prior to running numerical models or experiments. This method will also be applied to optimize the trap size for single particle immobilization which is important for cell printing and growth in a controlled fashion.

Theory

In this section, the theories of EWOD and DEP are explained. EWOD has been used to manipulate conductive droplets to specific electrodes based on the electrostatic forces.⁴¹ DEP has been used to manipulate the particles inside the droplet by changing their polarizability.

Electrowetting on dielectric (EWOD)

Lippmann first recognized the capillary rise of liquid in the presence of electric charges and laid the foundation of electrowetting on dielectric (EWOD) by introducing Lippmann law (eqn (1))⁴²

$$\gamma_{SL} = \gamma_{SDL} - \frac{c}{2} V^2 \quad (1)$$

in which, γ_{SL} is the solid–liquid interfacial tension when the voltage is applied; γ_{SLD} is the interfacial tension when there is no voltage; and c is the capacitance per unit area of the dielectric layer covering the electrodes in DMF. Berge combined Lippmann's law (eqn (1)) with Young's equation (eqn (2))³⁰ to relate the contact angle and the electric potential. This equation (eqn (3)) is referred to as Lippmann-Young equation (eqn (3)).⁴³

$$\gamma_{SL} = \gamma_{SG} - \gamma_{LG} \cos \theta \quad (2)$$

$$\cos \theta = \cos \theta_0 + \frac{1}{\gamma_{LG}} \frac{1}{2} C V^2 \quad (3)$$

In these equations, γ_{SG} is the solid–gas interfacial tension, γ_{LG} is the liquid–gas interfacial tension and θ_0 and θ are the contact angles without and with the voltage applied, respectively. Basically, by applying the voltage to the adjacent electrode, charges in the droplet accumulate at the liquid–solid–gas interface resulting in apparent reduction of liquid–solid interfacial tension. However, it must be mentioned that the change in the apparent contact angle after applying the voltage could be the side effect in EWOD. In essence, the driving force is the result of electrostatic forces, and hence the change in the wettability of the system is the side effect of the forces acting on the droplet.⁴⁴ The same physics applies to droplet transport in DMF where the droplet is in contact with the adjacent electrode. By applying the voltage, charges in the droplet travel to the three-phase contact line where the electrostatic forces pull the droplet toward the actuated electrode.

Another problem with the Lipmann-Young relation (eqn (3)) is that it does not reflect the effect of the frequency of the applied voltage on droplet actuation. In essence, the dielectric can be modeled as a capacitor for which the impedance is related to the frequency of the applied voltage (see eqn (4)).

$$Z_D = \frac{1}{2\pi C_D f} \quad (4)$$

In this equation, f is the frequency of the applied electric field and C_D is the capacitance of the dielectric layer. The droplet confined between the two plates can also be modeled as a parallel combination of a resistor and capacitor (see Fig. S1 in ESI†). The capacitance of the droplet and dielectric layer and the resistance of the droplet can be presented as

$$C_1 = \frac{\epsilon_0 \epsilon_r l A}{H} \quad (5)$$

$$C_D = \frac{\epsilon_0 \epsilon_r D A}{t} \quad (6)$$

$$R_l = \rho_l \frac{H}{A} \quad (7)$$

where ϵ_0 and ϵ_r are the vacuum and relative permittivity respectively; ρ is the resistivity; t is the thickness of the dielectric layer; H presents the gap between the top and bottom plates; and A is the area of the electrode. Liquid droplet and dielectric layer properties are shown with l and D indices, respectively.

Based on the model shown in Fig. S1, ESI† the voltage drop across the droplet and the dielectric layer can be calculated. Here, the equivalent impedance for the electrical model is $Z_{eq} = Z_d + (Z_L \times R_l)/(Z_L + R_l)$, and hence the drop of the voltage across the dielectric layer and the droplet are $V_D = V_{input}(Z_d/Z_{eq})$ and $V_l = V_{input} - V_D$, respectively. When a DC or low frequency AC voltage is applied between the top (containing a layer of conductive coating such as transparent ITO) and bottom plates, a main portion of the voltage will drop across the dielectric layer since the capacitor acts as an infinite

resistance (see eqn (4)) for the case of a zero (DC voltage) or low frequency AC signal. As a result, the electric field in the droplet becomes very weak and hence dielectrophoresis force will be negligible. For high frequency AC signals, on the other hand, the impedance of the dielectric layer diminishes (see eqn (4)) and electric field in the droplet will be stronger, resulting in a stronger dielectrophoresis force.

Fig. S2 (included in the ESI†) shows the voltage drop across the droplet with different conductivities over a range of applied frequencies. The values were calculated for the input voltage of 100 V. The figure shows that for the same voltage as the conductivity of the droplet increases, higher frequency is required to create the largest voltage drop across the droplet. In this paper, droplets of DI water (with low conductivity) were used. Based on the above figure, the frequency resulting in the largest voltage drop across the droplet (*i.e.*, 80 V) is above 30 kHz.

Dielectrophoresis (DEP)

Dielectrophoresis describes the force exerted by a non-uniform electric field on the polarizable particles.³³ The dielectrophoresis force can be derived from either the Maxwell stress tensor approach or the effective dipole moment approach.^{45,46} The Maxwell stress tensor approach can be considered as a rigorous and accurate method but fairly difficult to apply to a large number of circular-shape particles. The effective dipole moment approach, on the other hand, is simple to implement and computationally less expensive. In this approach, the dielectrophoresis force on a particle in a non-uniform electric field can be written based on the effective dipole moment and the electric field^{33,38}

$$\vec{F}_{\text{DEP}} = (\vec{p} \cdot \nabla) \vec{E} \quad (8)$$

where \vec{p} is the dipole moment vector and \vec{E} is the electric field. For a spherical small particle of a radius a , the electric field, \vec{E} , can be assumed to not change significantly over the surface of the particle. As a result, the dielectrophoresis force can be calculated based on

$$\vec{F}_{\text{DEP}} = 2\pi a^3 \varepsilon_m \text{Re}(f_{\text{CM}}) \nabla(|\vec{E}|^2) \quad (9)$$

where, ε_m is the relative permittivity of the suspending medium, $|\vec{E}|$ is the root mean square (rms) value of the non-uniform electric field, and $\text{Re}(f_{\text{CM}})$ is the real part of the Clausius-Mosotti (CM) factor.³³ The Clausius-Mosotti factor can be described as a function of the medium and the particle complex permittivities.

$$f_{\text{CM}} = \frac{\varepsilon_p^* - \varepsilon_m^*}{\varepsilon_p^* + 2\varepsilon_m^*} \quad (10)$$

In this relationship, ε_p^* and ε_m^* are the complex permittivities of the polarizable particle and the suspending medium, respectively. These two terms are frequency dependent and can be described as

$$\varepsilon_{p,m}^* = \varepsilon_0 \varepsilon_{p,m} - j \frac{\sigma_{p,m}}{2\pi f} \quad (11)$$

where ε_0 is the permittivity of the free space ($\varepsilon_0 = 8.854 \times 10^{-12} \text{ Fm}^{-1}$), f is the frequency of the applied electric field. Subscripts p and m denote the particle and the medium, respectively. The value of f_{CM} factor is limited within $-0.5 \leq f_{\text{CM}} \leq 1$ based on the frequency of the applied electric field.³³ When the value of f_{CM} is greater than zero, *i.e.* the polarizability of the particles is more than that of the surrounding media, the dielectrophoresis force manipulates the suspended particles towards the region with a maximum electric field intensity, which is referred to as positive DEP (pDEP). If the value of f_{CM} is less than zero, *i.e.* the medium is more polarizable than the particle, the dielectrophoresis force drives the particles towards the region with a minimum electric field intensity, which is referred to as negative dielectrophoresis (nDEP).

In this paper, the droplet contains DI water mixed with the polystyrene spherical beads (functionalized with the carboxyl group) with the diameter of 5 μm . Fig. S3 (included in ESI†) shows the real part of the f_{CM} factor calculated (using eqn (10)) for different frequencies for the system described above. For frequencies less than 1 kHz, the f_{CM} factor is positive so the particles are expected to travel to the high intensity field (*i.e.*, positive DEP); however, as the frequency increases, the f_{CM} factor becomes negative so that the particles are repelled from the high intensity zones (*i.e.*, negative DEP). In this paper, the working frequency is 30 kHz for the droplet containing DI water (as explained in the previous section). For this frequency, the particles are expected to experience negative DEP (see Fig. S3, ESI†).

Numerical

As it was discussed in the previous section, the particles will experience nDEP for frequencies more than 1 KHz. Therefore, the only way to capture them on the bottom plate is to create trap zones on the electrodes. These zones will have the low intensity electric field to capture the particles. One way to create these zones on the bottom plate is to apply a positive voltage to two adjacent electrodes that have sufficient distance from each other. Fig. S4 (included in the ESI†) presents the schematic of the system discussed. The same voltage is applied to the two adjacent bottom electrodes; while the top plate is grounded. A numerical model has been developed to study the particle migration to the trap zone (between the two bottom electrodes) due to the effect of nDEP. The geometry and boundary conditions for the model are shown in Fig. S4, ESI† To study the motion of the particles, the Laplace equation for the electrostatic condition of the electromagnetic field⁴⁷ is solved using the finite volume method.

$$\frac{\partial^2 \Phi(x,y,z)}{\partial x^2} + \frac{\partial^2 \Phi(x,y,z)}{\partial y^2} + \frac{\partial^2 \Phi(x,y,z)}{\partial z^2} = 0 \quad (12)$$

In this equation, Φ presents the electrostatic potential. For a simple geometry (such as Fig. S4, ESI†), the electric field is

solved at the meridian plane of the droplet (solving eqn (12) in a 2D domain). For more complex geometries (like square-shape or circular-shape traps) the above equation is solved in the 3D domain (see the numerical results in section 5). In this simulation, the particle–particle interaction is not considered. Also, the effect of polarization of the particle on the electric field is assumed to be negligible. The boundary condition chosen for the trap zone between two bottom electrodes is Neumann⁴⁷ which is a suitable boundary condition for the liquid–solid interface. The Neumann boundary condition is also applied to other boundaries in the Z-direction. Fig. S5 (a) (included in the ESI†) shows the results of the electric field value in the geometry shown in Fig. S4, ESI†. The result shows that the above electrode configuration creates an intense non-uniform electric field in the droplet. Also, the intensity of the electric field is maximum close to the edge of each electrode and is reduced to its minimum value at the middle of the gap between the two bottom electrodes. The simulation results presented in Fig. S5, ESI† (a) are non-dimensionalized based on the gap size between the top and bottom plates. Although varying the gap size will change the capacitance and the resistance of the of droplet (as described in section 2.1), the results in Fig. S5, ESI† (a) suggest that the general form of the electric field will remain the same (the high intensity electric field occurs at the edge of the electrodes and the low intensity zone happens in the middle of the space between electrodes).

Based on the values of the electric field, the program calculates the DEP force (using eqn (9)). Fig. S5, ESI† (b) (included in Electronic Supplementary Information) shows the negative dielectrophoresis force field between the top and bottom plates. Based on the direction of the DEP forces, it can be predicted that the particles move toward the bottom plate and trapped in the low intensity zone (the gap between the electrodes) far away from the edge of the electrodes. In essence, the Y-component of the DEP force at the middle is toward the bottom plate; whereas, near the edge of the electrodes, the vertical component of the forces is toward the top plate. As a result, along the gap between the two electrodes, a particle can experience two different forces: lifting and trapping. These forces identify two separate regions called trapping and lifting zones. The diameter of the particle and the size of the lifting and trapping zones (which depend on the electrode geometry) identify the position of the particles with respect to the bottom and top plates.

To predict the motion of the particles in the droplet, Newton's equation of motion is solved with the velocity Verlet algorithm.⁴⁸ In the simulation, 100 particles are considered and they randomly distributed in the domain. The top and bottom boundaries are considered as a reflective boundary.⁴⁸ The periodic boundary condition (PBC)⁴⁸ is applied to all other boundaries. The particles in the droplet experience three forces: DEP, viscous, and buoyancy forces. The DEP force is calculated based on eqn (5). The viscous drag force, \bar{F}_d , is calculated based on,⁴⁹

$$\bar{F}_d = -6\pi\mu a\bar{u}_p \quad (13)$$

where μ , a and \bar{u}_p are viscosity of the medium (droplet), diameter of the particle and velocity of the particle, respectively. The force of

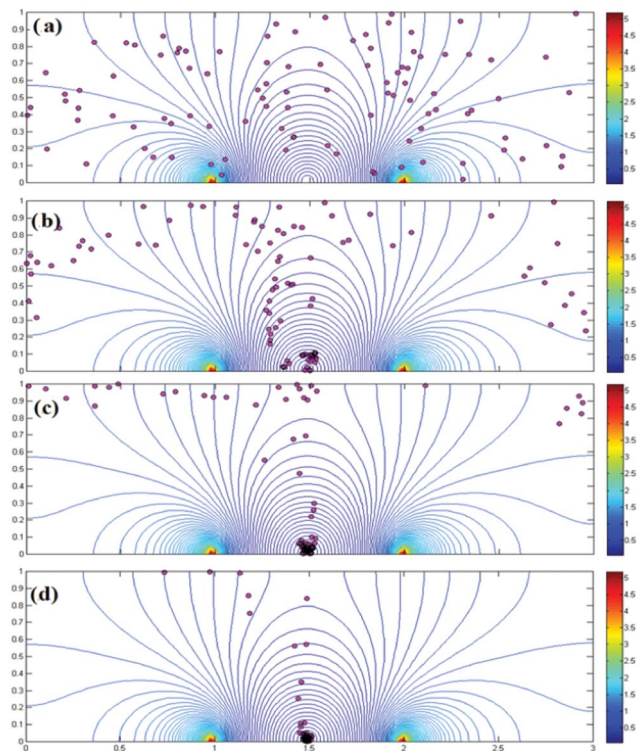


Fig. 1 Particle trajectory in the computational domain is shown. The particles exposed to the nDEP force are shown at different instants: (a) initial condition of the particles in the domain, (b) position of the particles after 5 s, (c) position after 40 s, and (d) position after 120 s.

buoyancy, \bar{F}_b , is considered as

$$\bar{F}_b = m_p \bar{g} (1 - \rho_m / \rho_p) \quad (14)$$

where m_p , ρ_p , ρ_m present the mass of the particle, and the density of the particle and the medium, respectively. Fig. 1 shows the result of the numerical simulation tracking the particle motion at each instant. The results are presented for particles with the diameter of 5 μm . By applying the nDEP force the particles that are at the vicinity of the trap zone (i.e., between the two electrodes) travel to the trap in a relatively short time. However, the particles that are originally far away from the trap zone will first move upwards (away from the trap) and then travel towards the trap zone due to the direction of the DEP force shown in Fig. S5 (b), ESI†.

Experiments were also conducted to validate the numerical results. Fig. S6 (included in the ESI†) shows the droplet containing polystyrene beads with a diameter of 5 μm and concentration of approximately 1500 particles μL^{-1} . The droplet was actuated using EWOD to adjacent electrode with a striped design which is used for particle trapping based on nDEP. A DC voltage of 150 volts was applied for droplet actuation. Then, by applying an AC voltage of 100 Vpp at 30 kHz, the particles move to the traps in the middle of the two striped electrodes. The time required for almost all of the particles to travel to the traps is around 2 min which matches with traveling time obtained from simulation for 100 particles.

This suggests that the time required for trapping does not depend on the particle concentrations.

The simulation and the experimental results obtained for the striped electrodes demonstrate the concept of nDEP used for trapping. In the striped-shape traps the particles are lined up creating a chain which may not be desirable when exact positioning of the particles (*e.g.*, for cell culture³⁴) or controlling the number of trapped particles is of interest. Thus, confined geometries must be characterized to find the optimum trap dimensions for capturing a desired amount of particles of a given diameter. In this paper two confined geometries including circular and square shapes are studied for this purpose.

Experimental

Design and fabrication

A parallel plate testing device was fabricated on the glass substrate using standard micro-fabrication techniques. At first, a copper layer with the thickness of 45 nm was sputtered onto the bottom glass substrate (using Nexdep deposition system, Angstrom Engineering Inc.). Using the standard photolithography technique, the patterns were created on the bottom plate. A layer of photoresist S1813 (MicroChem Corp.) was spun at 3000 rpm and then post-baked for 60 s. A subsequent UV exposure and a mask were applied to create the required patterns on the chip. The substrate was then developed using the MF-319 developer. A diluted ferric chloride solution was used as the copper etchant. The remaining photoresist was removed using acetone. For creating the dielectric layer, S1813 was spun at a speed of 4000 for 60 s on the patterned chip and baked at 95 °C for 30 min. Finally, Teflon AF 1600 (DuPont) at the concentration of 3 wt% was spun on top of the dielectric layer at a speed of 2500 rpm for 60 s.

A transparent ITO coated glass substrate (SiO₂ passivated, $R_s = 4\text{--}8\ \Omega$) was used as the top plate facilitating visualization of particle motion. The ITO surface was then coated with Teflon (following the procedure explained above) to increase the hydrophobicity of the surface. A constant gap of 240 μm between the two plates was maintained using spacers. Finally, the driving electrodes were connected to wires using an adhesive conducting gel. The electrical potential was applied using a signal generator (Tektronix AFG3021B0) connected in series with an amplifier (TREK PZD700). An Apo-zoom microscope (Leica Z6 APO) connected to a high speed camera, acquiring 30 frames/s with the resolution of 2592×1944 , was used to monitor the motion of the particles from the transparent top plate. The camera is equipped with $10\times$ optical lens providing images with higher magnification required for tracing particle motion. The optical system was calibrated using a calibration grid pattern converting pixels to centimeters.⁵¹ All the measurements were repeated three times to ensure reproducibility.

Sample preparation

Polystyrene microbeads (also referred to as particles in this paper) with a mean diameter of 5.01 μm and density of 1.05 g cm^{-3} (PS/7%DVB5%MAA, purchased from Bangs Laboratories Inc.) were suspended in DI water. The beads have carboxylic surface functional groups. The conductivity of the solution was measured as 8.6 $\mu\text{S cm}^{-1}$ (at 25 °C). For this study, a 1 μl droplet containing the beads with the concentration of 1500 particles/ μl was dispensed on the spatial electrodes which were used to transfer the droplet to the trapping electrode by EWOD.

Results

A series of simulations and experiments were conducted to identify lifting and trapping zones for the two geometries studied here (see section 5.1). This will result in finding a correlation between the geometrical factors including the size of the traps and particles with respect to the number of the particles captured. This relationship will be used to find the dimensions required for single trapping (see section 5.2)

Characterization of trapping zones

Fig. 2 shows an array of square shape spaces (with the width of $W = 90\ \mu\text{m}$) on the bottom electrode for capturing polystyrene beads. Before applying the voltage, the particles are scattered throughout the liquid droplet. As the voltage is turned on (100 Vpp at 30 kHz), the polystyrene beads are drawn to the middle of the square space (*i.e.*, trapping zone). Over time the concentration of the particles in the trap region increases until a saturation point at which there is no space left to accept a new particle. After this saturation point, the particles will stack on the first layer formed on the trap zone. The capture process will continue until all particles are moved toward the trap. The transient change in the width of the covered area (S) (the area of the space that is covered with the particles) for the square-shape spaces with the widths of $W = 90\ \mu\text{m}$ and $W = 60\ \mu\text{m}$ are shown in Fig. 3a. The width of the covered area is calculated based on the average covered area ($S = (\text{average covered area})^{1/2}$). In the experiments presented here, nearly all the beads were captured on the trapping zones within approximately 2 min. However, the duration of the experiments was extended to 5 min to ensure that all the particles were captured. It is worth to mention that as soon as the voltage is turned off, the particles start to disperse inside the droplet.

The width of the area covered with particles was also used as a parameter to quantify the particle captured on the trap zones since it is impossible to measure the exact number of the particles as they may have stacked on each other. This trapping zone takes the shape of the space created in the electrode due to the equal electric field contribution from each side. Outside of the trapping region, a strong electric field gradient is present. It has experimentally been observed that

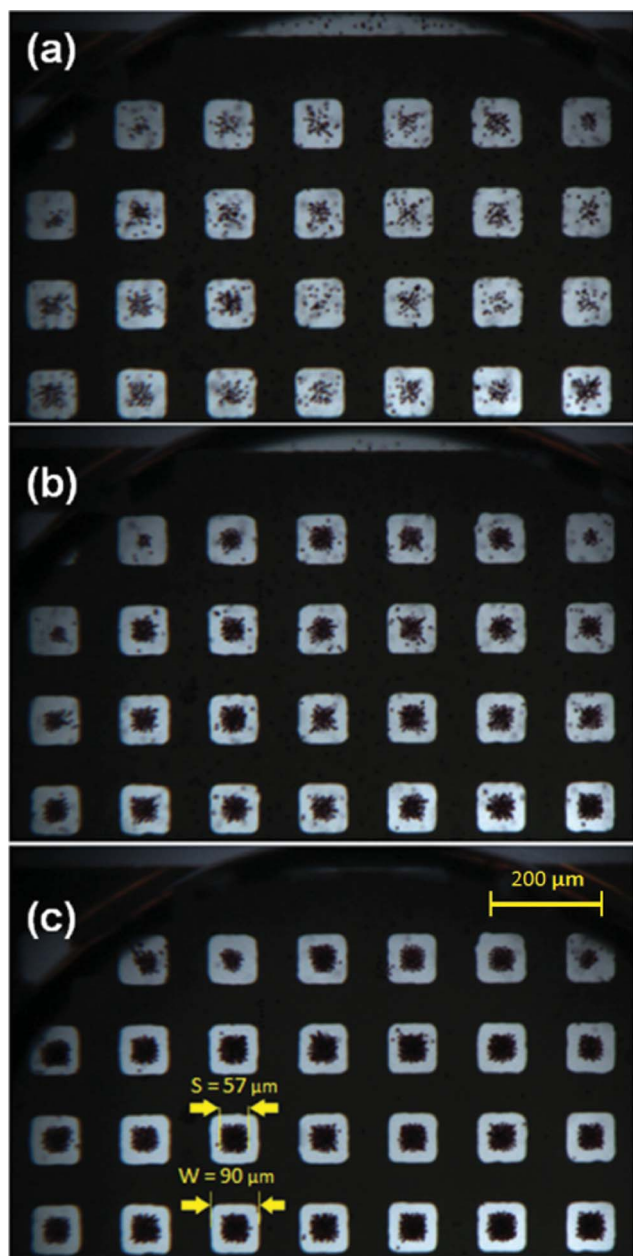


Fig. 2 Particle trapping on square-shape traps after applying voltage for (a) 5 s, (b) 30 s, and (c) 5 min.

the polystyrene beads do not settle down in this zone, which is referred to as a lifting zone, as they are repelled from the edge of the electrode.

The experiments with the square-shape space were repeated for different dimensions ranging from 40 to 90 μm . For each dimensions, experiments were repeated three times to ensure reproducibility of the results. In each experiment, the width of the trapping zone (S) was measured and compared to the total dimension of the space (W) to obtain the percentage of the trapping zone over the lifting zone (see Fig. 3b). It was observed that regardless of the size of the space, the trapping

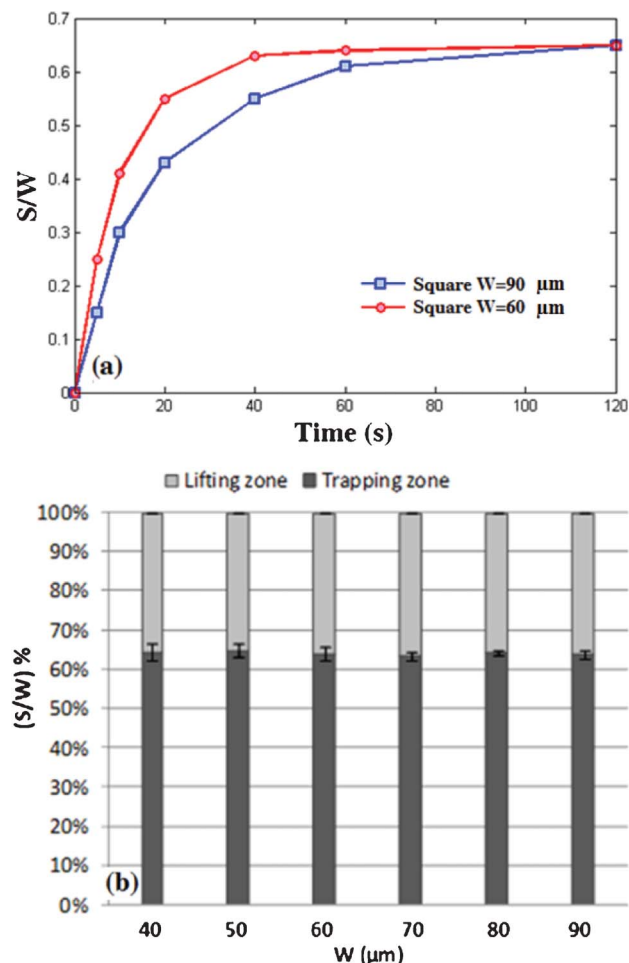


Fig. 3 (a) Transient change in the covered area for square-shape space, (b) experimental comparison between trapping and lifting zones for the square shape trap spaces.

zone is approximately 63% of the total space for the range of the spaces studied experimentally.

Since fabrication of a square-shape space with the width less than 40 μm was not possible (the corners of the squares become rounded in the etching process), a numerical simulation, based on eqn (9) and (12), was developed to determine the trapping area percentage for smaller shapes. In essence, the size of the trapping and lifting zones is calculated based on the direction of the Y-component of the DEP force. If the force is toward the bottom plate it is considered as the trapping zone; whereas the opposite direction is considered as the lifting zone. The numerical results (see Fig. 4) show that for the square-shape space smaller than 40 μm , the size of the covered area decreases by decreasing the space size; whereas for the spaces larger than 40 μm the trapping area remains constant similar to the experimental results. In essence, for the space width less than 40 μm the magnitude of the electric field (affected by the geometry) and consequently the size of the trapping zone decrease.

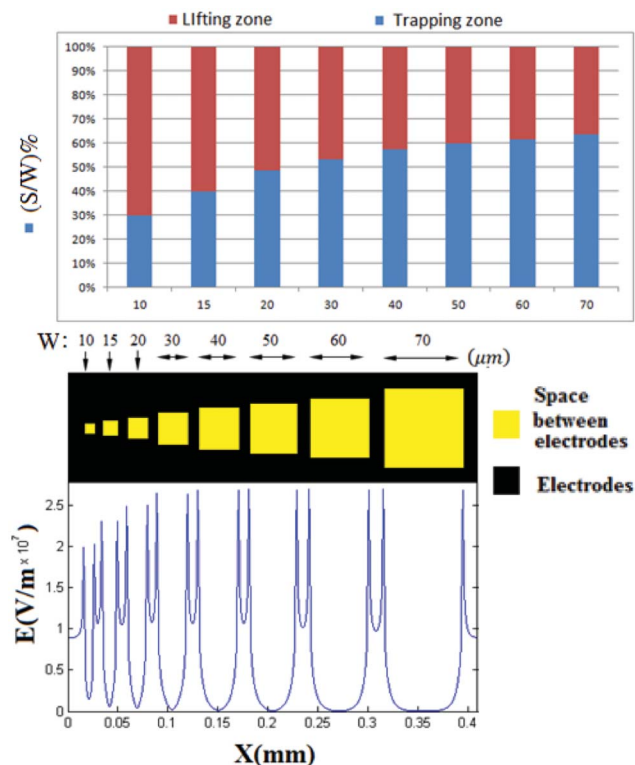


Fig. 4 Trapping and lifting zone percentages obtained numerically for different square-shape trap sizes are shown. Electric field profile for different trap sizes are presented

Similar experiments were conducted for circular traps. Fig. S7 (included in the ESI†) shows particle trapping in an array of circular gaps. Like the previous case, a voltage of 100 Vpp at 30 kHz has been applied. Due to the strong electric field gradient at the edge, particles were observed to experience the repelling force which manipulated them towards the area of the minimum electric field gradient in the middle. As a result, the particles cover a circular area (see Fig. S7c, ESI†). The transient change in the diameter of the covered area (S) (the area of the space that is covered with the particles) for the circular-shape spaces are shown in Fig. S8a (included in the ESI†). The diameter of the covered area for the circular-shape space is calculated on the average covered area ($S = (4 \times \text{average covered area} / \pi)^{1/2}$). Fig. S8b, ESI† shows a comparison of the trapping zone and lifting zone obtained through experiments for a range of circular spaces. It is observed that for the diameters ranging from 50 to 100 μm, the trapping zone is constant, and similar to the square-shape traps is around 63% of the total space diameter. Below 35 μm, however, the size of the trapping zone decreases as the diameter of the circular space decreases. The electric profiles for the circular space and for different space size are presented in Fig. S9 (included in the ESI†). It is observed that by reducing the diameter of the space the electric field gradient becomes more intense and the area with low gradient in the middle shrinks.

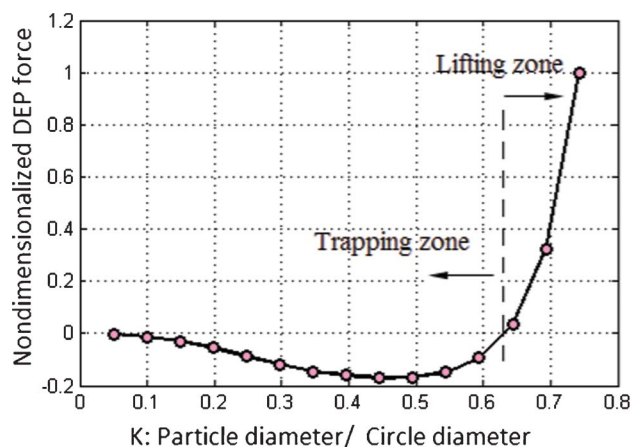


Fig. 5 Normalized DEP force as a function of the particle diameter to the trap size ratio ($K = \frac{D}{W}$) is presented. For trapping the particles, K must be less than 0.63.

Single particle trapping

In the previous section, the experimental and numerical results show that there is a relationship between the space dimension (either in the form of the width of the square shape or diameter of the circular shape) and the trapping zone area. This relationship can be very useful in identifying, for instance, the size of the space required for trapping a single particle of a certain diameter. This space size can basically be obtained by multiplying the trapping zone percentage by the width (or diameter) of the space. For instance, in the case of the circular shape (see Fig. S8, ESI†), a space with a diameter of approximately 15 μm is required to trap a single particle with the diameter of 5 μm. To verify this fact, an experiment was conducted in which circular spaces with the diameters of approximately 15 μm were fabricated (see Fig. S10 in the ESI†). This dimension facilitates the capture of a single particle. Also, as it was explained in the previous section, for the space size bigger than 40 μm, the size of the trapping area to the space size is almost constant and approximately is equal to 63% regardless of the shape of the capturing space. This can be used to define a limiting constant, K , which can identify the status of particle trapping prior to running numerical models or experiments. In essence, K is defined based on the ratio of the particle diameter to the dimension of the space. Fig. 5 shows the Y-component of the normalized DEP force at the trapping zone that is numerically calculated as a function of K for different particle diameters. This plot can be used as a design tool to select the space dimension for trapping a certain size of particles. From the graph, it can be concluded that when the value of $K \approx 0.63$, a particle will experience the minimum force that can hold it in the trap. Beyond this value of K , DEP force will levitate the particle towards the bulk. This can explain the experimental results obtained for the square and circular space arrays.

Conclusions

In this paper, the effect of nDEP trap geometry on particle capture in a digital microfluidic platform has been studied

experimentally and numerically. It has been demonstrated that regardless of the trap shape there is a specific trap size less than which particles cannot settle down. As a result, lifting and trapping zones have been introduced based on simulation and experimental results which used to define a limiting constant K identifying the status of particle trapping. The experimental results were also used to find the size of the nDEP trap for capturing a single particle. This study can be used to design trap geometries for applications requiring high capture efficiency (e.g., waterborne pathogen detection) or single particle immobilization (e.g., cell growth).

References

- 1 A. H. C. Ng, K. Choi, R. P. Luoma, J. M. Robinson and A. R. Wheeler, *Anal. Chem.*, 2012, **84**, 8805–8812.
- 2 D. Bogojevic, M. D. Chamberlain, I. Barbulovic-Nad and A. R. Wheeler, *Lab Chip*, 2012, **12**, 627–634.
- 3 J. Fu, R. B. Schoch, A. L. Stevens, S. R. Tannenbaum and J. Han, *Nat. Nanotechnol.*, 2007, **2**, 121–128.
- 4 Y. Kang, D. Li, S. Kalams and J. E. Eid, *Biomed. Microdevices*, 2008, **10**, 243–249.
- 5 S. K. Srivastava, P. R. Daggolu, S. C. Burgess and A. R. Minerick, *Electrophoresis*, 2008, **29**(24), 5033–5046.
- 6 N. M. Jesús-Pérez and B. H. Lapizco-Encinas, *Electrophoresis*, 2011, **32**(17), 2331–2357.
- 7 J. Castillo, M. Dimaki and W. E. Svendsen, *Integr. Biol.*, 2009, **1**, 30–42.
- 8 C. L. Asbury, A. H. Diercks and G. van den Engh, *Electrophoresis*, 2002, **23**, 2658–2666.
- 9 R. B. Fair, A. Khlystov, T. D. Taylor, V. Ivanov, R. D. Evans, V. Srinivasan, V. K. Pamula, M. G. Pollack, P. B. Griffin and J. Zhou, *IEEE Des. Test Comput.*, 2007, **24**, 10–24.
- 10 H. Gardeniers and A. V. Den Berg, *Int. J. Environ. Anal. Chem.*, 2004, **84**, 809–819.
- 11 R. Kretschmer and W. Fritzsche, *Langmuir*, 2004, **20**(26), 11797–11801.
- 12 K. Dholakia, P. Reece and M. Gu, *Chem. Soc. Rev.*, 2008, **37**, 42–55.
- 13 J. Z. Chen, S. M. Troian, A. A. Darhuber and S. Wagner, *J. Appl. Phys.*, 2005, **97**, 014906–014909.
- 14 A. Wixforth, C. Strobl, C. Gauer, A. Toegl and J. Scriba, *Anal. Bioanal. Chem.*, 2004, **379**, 289–291.
- 15 J. Gong and C. J. Kim, *Lab Chip*, 2008, **8**, 898–906.
- 16 J. A. Schwartz, J. V. Vykoukal and P. R. C. Gascoyne, *Lab Chip*, 2004, **4**, 11–17.
- 17 Z. G. Guo, F. Zhou, J. C. Hao, Y. M. Liang, W. T. S. Huck and W. M. Liu, *Appl. Phys. Lett.*, 2006, **89**, 081911–081913.
- 18 A. Ahmadi, *PhD thesis*, University of British Columbia, 2011.
- 19 D. G. Grier, *Nature*, 1995, **378**, 810–816.
- 20 G. J. Shah, A. T. Ohta, E. P.-Y. Chiou, M. C. Wu and C. J. Kim, *Lab Chip*, 2009, **9**, 1732–1739.
- 21 T. Laurell, F. Petersson and A. Nilsson, *Chem. Soc. Rev.*, 2007, **36**, 492–506.
- 22 M. Lian, N. Islam and J. Wu, *IET Nanobiotechnol.*, 2007, **1**(3), 36–43.
- 23 Y. Wang, Y. Zhao and S. K. Cho, *J. Micromech. Microeng.*, 2007, **17**, 2148–2156.
- 24 R. Sista, Z. Hua, P. Thwar, A. Sudarsan, V. Srinivasan, A. Eckhardt, M. Pollack and V. Pamula, *Lab Chip*, 2008, **8**, 2091–2104.
- 25 R. Sista, A. Eckhardt, V. Srinivasan, M. Pollack, S. Palanki and V. Pamula, *Lab Chip*, 2008, **8**, 2188–2196.
- 26 Y. Wang, Y. Zhao and S. K. Cho, *J. Micromech. Microeng.*, 2007, **17**, 2148–2156.
- 27 G. J. Shah and C. J. Kim, Meniscus-assisted high-efficiency magnetic collection and separation for EWOD droplet microfluidics, *J. Microelectromech. Syst.*, 2009, **18**, 363–375.
- 28 D. Di Carlo, L. Y. Wu and L. P. Lee, *Lab Chip*, 2006, **6**, 1445–1449.
- 29 T. Endo, A. Okuyama, Y. Matsubara, K. Nishi, M. Kobayashi, S. Yamamura, Y. Morita, Y. Takamura, H. Mizukambi and E. Tamiya, *Anal. Chim. Acta*, 2005, **531**, 7–13.
- 30 M. J. Schertzer, R. Ben-Mrad and P. E. Sullivan, *J. Microelectromech. Syst.*, 2011, **20**, 1010–1015.
- 31 S. K. Cho and C. J. Kim, *Proceedings IEEE Sixteenth Annual International Conference on Micro Electro Mechanical Systems*, 2003, 686–689.
- 32 C. Zhang, K. Khoshmanesh, A. Mitchell and K. Kalantar-Zadeh, *Anal. Bioanal. Chem.*, 2010, **396**, 401–420.
- 33 T. B. Jones, *Electromechanics of Particles*, Cambridge University Press, Cambridge, 1995.
- 34 R. Thomas, H. Morgan and N. Green, *Lab Chip*, 2009, **9**, 1534–1540.
- 35 G. Medoro, N. Manaresi, A. Leonardi, L. Altomare, M. Tartagni and R. Guerrieri, *IEEE Sens. J.*, 2003, **3**, 317–325.
- 36 T. Schnelle, R. Hagedorn, G. Fuhr, S. Fiedler and T. Müller, *Biochim. Biophys. Acta, Gen. Subj.*, 1993, **1157**(2), 127–140.
- 37 A. Rosenthal and J. Voldman, *Biophys. J.*, 2005, **88**(3), 2193–2205.
- 38 D. F. Chen, H. Du and W. H. Li, *Sens. Actuators, A*, 2007, **133**(2), 329–334.
- 39 N. Lewpiriyawong, K. Kandaswamy, C. Yang, V. Ivanov and R. Stocker, *Anal. Chem.*, 2011, **83**(24), 9579–9585.
- 40 S. K. Fan, P. W. Huang, T. T. Wang and Y. H. Peng, *Lab Chip*, 2008, **8**, 1325–1331.
- 41 T. B. Jones, *Langmuir*, 2002, **18**, 4437–4443.
- 42 J. Berthier, *Microdrops and Digital Microfluidics*, William Andrew Inc., New York, 1st Ed., 2008, 161–166.
- 43 J. Lee, H. Moon, J. Fowler, T. Schoellhammer and C. J. Kim, *Sens. Actuators, A*, 2002, **95**, 259–268.
- 44 K. Choi, A. H. C. Ng, R. Fobel and A. R. Wheeler, *Annu. Rev. Anal. Chem.*, 2012, **5**, 413–40.
- 45 T. Schnelle, T. Müller, C. Reichle and G. Fuhr, *Appl. Phys. B: Lasers Opt.*, 2000, **274**, 267–274.
- 46 X. Wang, X. B. Wang and P. R. C. Gascoyne, *J. Electrostat.*, 1997, **39**, 277–295.
- 47 C. H. Kua, Y. C. Lam, C. Yang, K. Youcef-Toumi and I. Rodriguez, *J. Electrostat.*, 2008, **66**, 514–525.
- 48 S. M. Mirnouri, L. M. Ghassemi, A. Shahabi and H. Rezaei Nejad, *J. Mol. Liq.*, 2011, **161**(2), 85–90.
- 49 Y. Lin, G. Amberg, F. Aldaus and J. Roeraade, Simulation of dielectrophoretic motion of microparticles using a molecular dynamics approach, *AIP Conf. Proc.*, 2006, **47608**, 1–10.
- 50 W. C. Nelson and C. J. Kim, *J. Adhesion Sci. Technol.*, 2012, **26**, 1747–1771.
- 51 M. Hoorfar and A. W. Neumann, *Adv. Colloid Interface Sci.*, 2006, **121**, 25–49.